Figure 1. Instrumental set-up. (a) Summary of the on-chip multi-imaging flow cytometry system. The system was composed of seven major modules: (i) microchip, (ii) bright-field (BF) imaging, (iii) fluorescent (FL) detection, (iv) multi-view, (v) CCD camera, (vi) sorting, and (vii) controller, as numbered in the figure. (b) Summary of the multi-view module. (c) A photograph of the system.
doi:10.1371/journal.pone.0104372.g001

Results

Development of on-chip multi-imaging flow cytometry system

The on-chip multi-imaging flow cytometry system (Fig. 1) was composed of seven major modules as an improvement of previous systems [11–13,26]: (i) microchip, (ii) bright-field (BF) light source, (iii) fluorescent (FL) excitation and detection, (iv) multi-view, (v) CCD camera, (vi) sorting, and (vii) controller, as numbered in Fig. 1 (a). In the BF light source module, an LED (625 nm wavelength) was used as a source for taking BF images and was irradiated from the top of the chip. This allowed simultaneous measurements of both BF and FL images, avoiding interference of the wavelengths during the measurements. An objective lens having 20× magnification and a 0.75 numerical aperture was set to the system, which allowed clear cell images to be taken within the depth range of the microchannel (25 μm) [27]. The FL excitation and detection modules contained three excitation lasers (375, 488, and 515 nm) and photomultipliers (PMTs), respectively, to monitor three different FL signals, which allowed conventional FL detection with labeling of target biomarkers. The controller module consisted of two independent units: one calculated FL signals and the other processed imaging biomarkers in multi-view

images. Maximum frequencies of calculations were 10,000 frequencies per second (fps) for controller 1, which calculated FL intensities, and 200 fps for controller 2, which processed imaging biomarkers for the current system. According to the adjustment of suitable thresholds for these parameters, feedback signals could be sent to the sorting module. The sorting module was composed of a direct current (DC) source and electrodes connected with a microchip, and could apply DC voltages to cells flowing in a microchannel of the chip to purify target cells under feedback signals, if necessary. Figure 1 (b) shows the principle of the multi-view module [27,28] used in this study. Firstly, optical paths between BF (red) and FL (blue) lights were separated using dichroic mirror A, as indicated in the figure. Next, angles of mirrors A and B were adjusted; then, BF and FL images were projected onto each half of a CCD component in the camera. An overview of the total system is shown in Fig. 1 (c). The system has a desktop size of 60 cm×60 cm.

Figure 2 shows the microchip designed to be suitable for this study. The chip body was fabricated with poly(dimethylsiloxane) (PDMS) attached to a cover glass to apply optical transparency in the observation. Microchannels were placed between the PDMS and the bottom cover glass in the chip with a 2 mmφ buffer entrance penetrating the PDMS. The upper stream of the
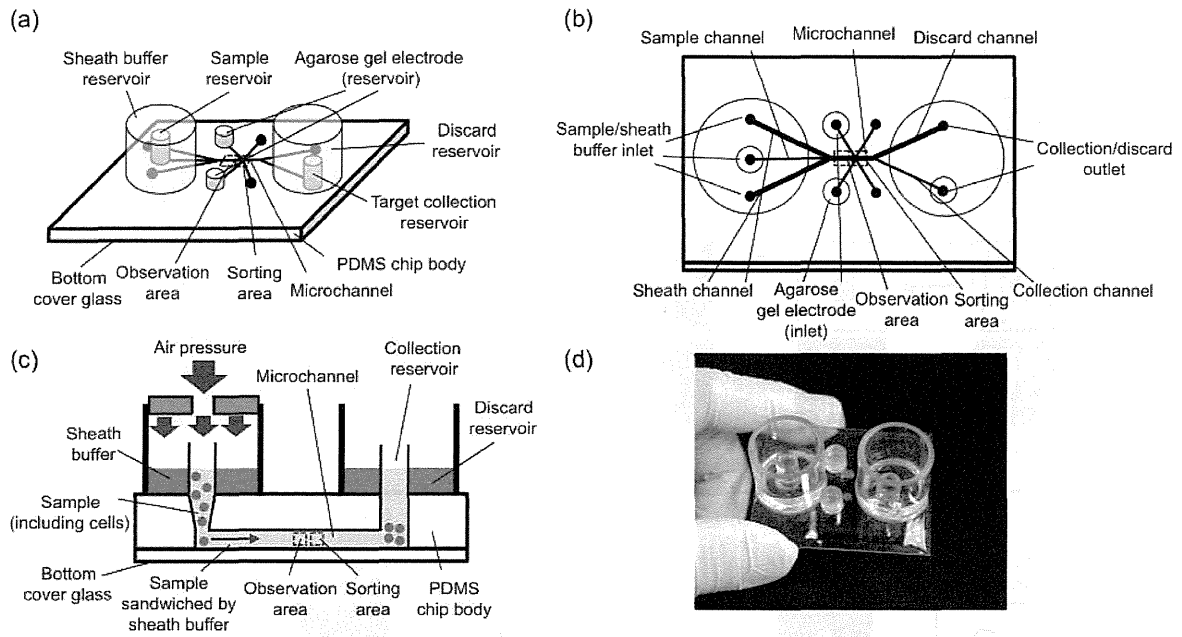
(a)

Sheath buffer reservoir
Sample reservoir
Agarose gel electrode (reservoir)
Discard reservoir
Target collection reservoir
PDMS chip body
Bottom cover glass
Observation area
Sorting area
Microchannel

(b)

Sample channel
Microchannel
Discard channel
Sample/sheath buffer inlet
Collection/discard outlet
Sheath channel
Agarose gel electrode (inlet)
Observation area
Sorting area
Collection channel

(c)

Air pressure
Microchannel
Collection reservoir
Discard reservoir
Sheath buffer
Sample (including cells)
Bottom cover glass
Sample sandwiched by sheath buffer
Observation area
Sorting area
PDMS chip body

(d)

Figure 2. Overview of the microchip. (a) Diagonal, (b) top, and (c) side views of the microchip used in this study. (d) A photograph of the chip. Total chip size is 50 mm×40 mm.
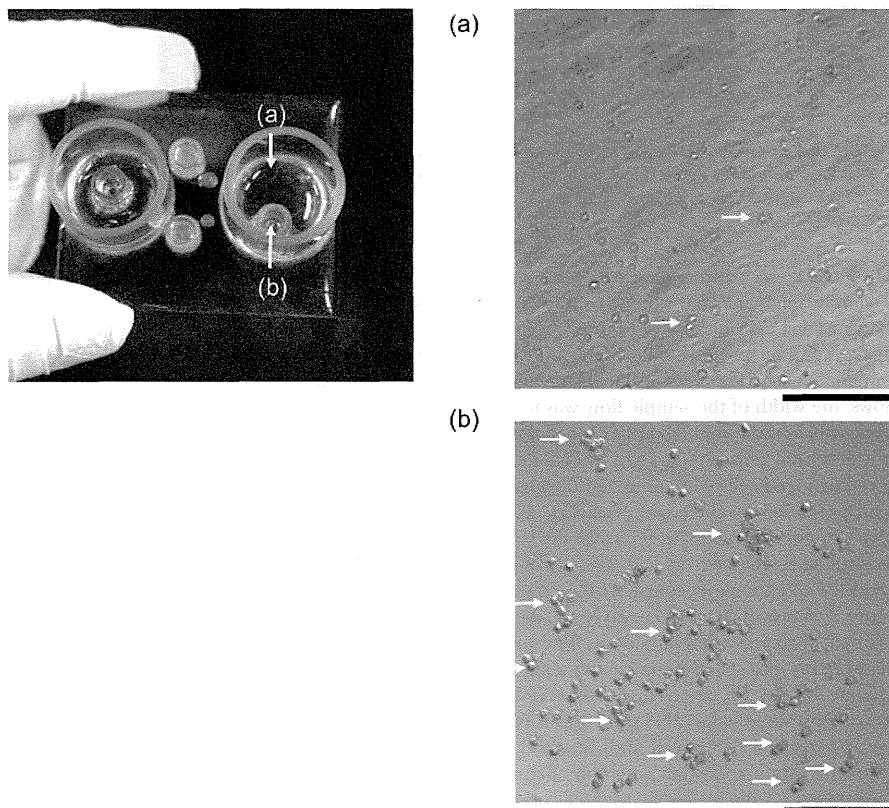doi:10.1371/journal.pone.0104372.g002

(a)

(b)

(a)

(b)

Figure 3. An example of cell sorting. Two photographs of the discarded reservoir (a) and the collection reservoir (b) indicated in the chip photograph are shown. Clustered cells are indicated by white arrows. Bars, 100 µm.
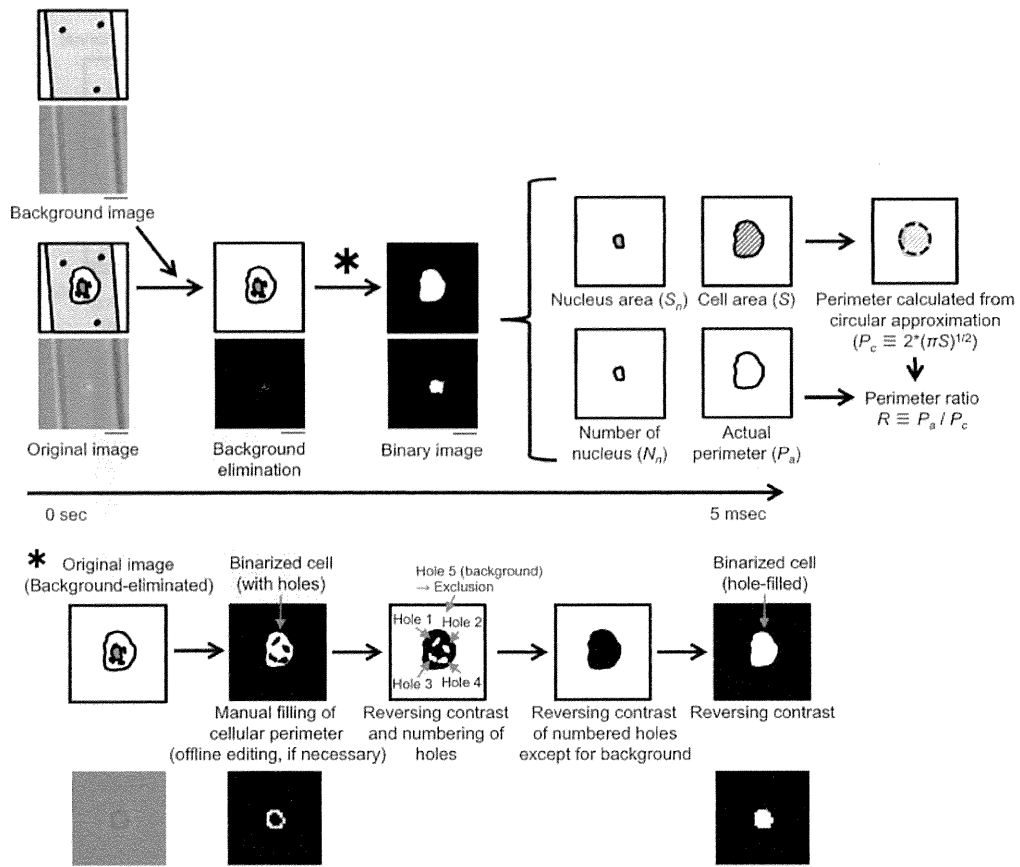doi:10.1371/journal.pone.0104372.g003

Figure 4. Summary of image processing. Firstly, photographs of both a cell and the background were taken. Next, the background image was subtracted from the cell image and holes were filled. Finally, imaging biomarkers, S, S_n, N_n, and R, were calculated. Bars, 10 μm. The hole-filling procedure is explained as indicated by an asterisk. Bar, 10 μm.
doi:10.1371/journal.pone.0104372.g004

microchannel was branched into three channels: the center connected with the sample inlet and the others were a sheath buffer inlet. Both sample and sheath buffers were introduced into the channel with application of air pressure onto both sample and sheath buffer inlets, simultaneously (Fig. 2 (c)). After the meeting of sample and sheath flows, the width of the sample flow was focused in the central one-third, which allowed imaging of each single cell upon the arrangement of all the cells in a straight line.

Images of the linearly arranged cells were obtained through the multi-view module and processed by the system (see Fig. 1), and when a target cell was found, DC voltage (typically 40 V with 100 μsec length) was applied to the cell through the agarose gel electrode (Fig. 2 (a) and (b)) to change its course in the collection channel [11,13]. Figure 3 shows a typical example of the cell sorting with a blood sample of a cancer-implanted rat. As shown in this figure, target cells were set into cell clusters having a large BF area, and once the value of the BF area of the observed cell exceeded the pre-adjusted threshold value, 300 μm² in this model case, a sorting voltage was applied to the cell and, finally, target cells were collected into the target collection reservoir. Figures 3 (a) and (b) show pictures taken for discarding (a) and collection (b) reservoirs, respectively. As shown in Fig. 3 (b), large cell clusters (indicated by arrows in the figures) were collected into the collection reservoir. On the other hand, single cells or small cell clusters were collected into the discarding reservoir (Fig. 3 (a)),

indicating the success of target collection using one imaging biomarker, BF area, as a collection parameter. The sorting capacity, which has been determined as the ratio between the number of target cells automatically detected by the system and the actual number of cells in the collection reservoir, was 24%. The low capacity of target cell collection was caused by the higher threshold setting in both recognition and collection processes to prevent 'false positive' sample collection. When the commercially available microbeads were used as a model target in this system, sorting capacity increased to 91%.

As shown in Fig. 3, target cells can be recognized by comparison of the imaging biomarkers with the threshold values pre-adjusted in the system. Figure 4 shows the detail of image processing in the system to obtain imaging biomarkers. Firstly, a background image, which was taken before the assay of flow cytometry, was subtracted from the obtained image with reductions of 8-bit grayscale values in each pixel. Next, the subtracted image was transformed to a binary image using a suitable threshold and pixel errors in the cell, which appeared by almost the same contrast in the cell as in the background, were filled (Fig. 4, asterisk); then, an extracted cell image was obtained. Finally, imaging biomarkers were calculated from the extracted cell image. In the current system, cell area (S) and actual perimeter (P_a) were obtained from the BF image, and nucleus area (S_n) and number of nuclei (N_n) were obtained from the FL image.
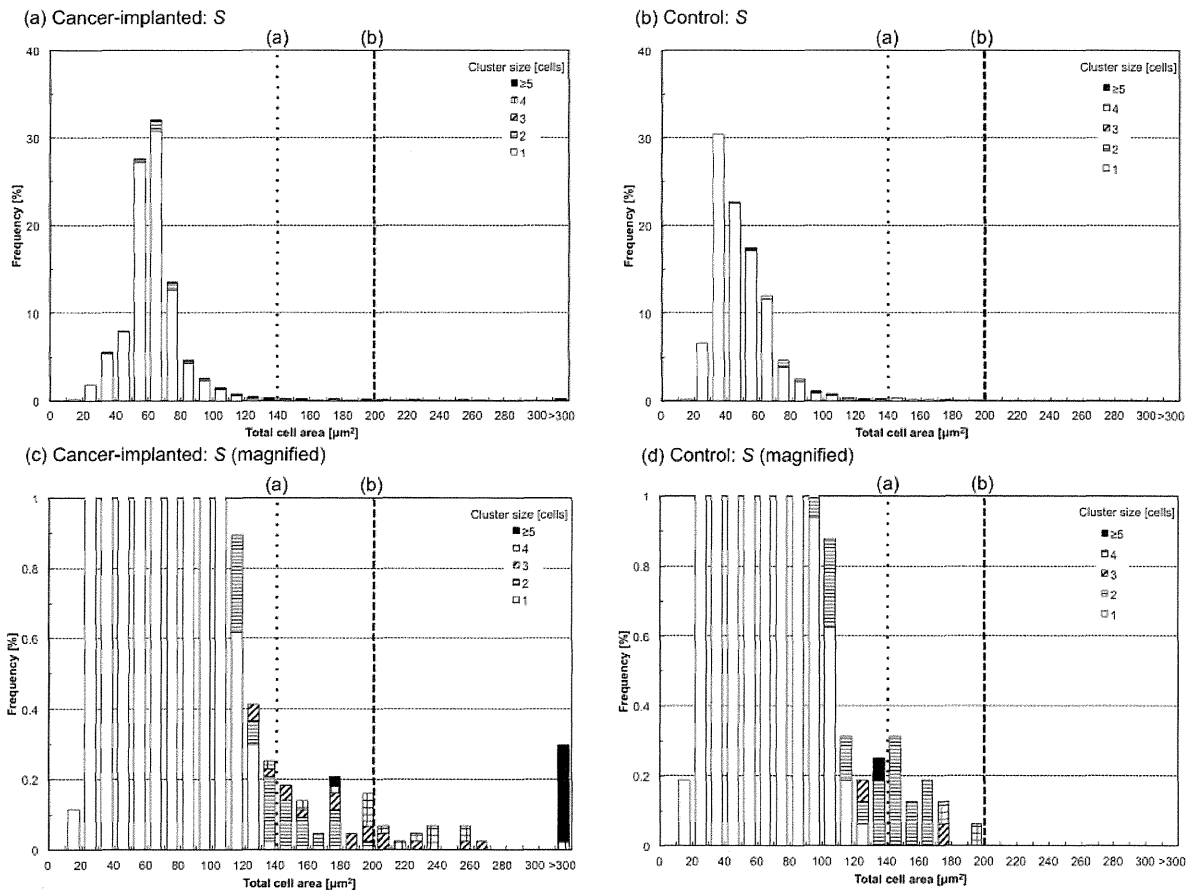
Figure 5. Histograms of total cell area, S, for cancer cell-implanted (a and c) and control blood (b and d). Two threshold values (a) and (b) for cluster identifications are indicated as dotted and dashed lines.
doi:10.1371/journal.pone.0104372.g005

Additionally, the perimeter ratio, R, which was obtained as the ratio between P_a and the perimeter calculated from S (P_c) [29], was also obtained. These calculations were performed in real time at 200 fps using controller 2 in Fig. 1, and in this study, manual calculations of the imaging biomarkers, including a few modifications for apparently failed auto-calculations caused by the failure of continuous detection of the cell perimeter in the hole filling procedure, were also performed as post-processing to confirm the reliabilities of the obtained imaging biomarker values.

Detection of clustered cells in cancer-implanted rat blood using imaging biomarkers

After the success of the system development, its performance for the identification of specific target cells using imaging biomarkers was quantitatively evaluated. Blood of a rat in which a rat prostate cancer cell line (MAT-LyLu) had been implanted was chosen as a model sample, and clustered cells in the blood were set as a target for the detection using imaging biomarkers with the developed system. One approach anticipated to achieve successful detection of the clusters is the use of cell area; therefore, areas in BF images (i.e., total cell area, S) and FL images (i.e., total nucleus area, S_n) were measured using the system. Figures 5 and 6 are histograms of S (Fig. 5) and S_n (Fig. 6) for cells in the cancer-implanted blood ($N = 4375$), shown with healthy rat blood as its control ($N = 1599$).

Detailed numbers including S and S_n are also summarized in Table 1. From the results, clustered cells were observed at a count of 237 in cancer-implanted samples (5.4% of the total) and a count of 56 in the control (3.5% of the total). In addition, two clear threshold values were found in both S and S_n; that is, (a) all cells having S larger than 140 μm^2 (count of 61, 1.4% of the total, for cancer-implanted samples and 13, 0.8% of the total, for the control) and S_n larger than 80 μm^2 (count of 34, 0.8% of the total, for cancer-implanted samples and 1, 0.1% of the total, for the control) were clustered cells, as indicated by the dotted lines in Figs. 5 and 6, and (b) the clustered cells having S larger than 200 μm^2 (count of 27, 0.6% of the total) and S_n larger than 90 μm^2 (count of 26, 0.6% of the total) were specifically observed in cancer cell-implanted blood. These results indicate that some cell clusters can be identified by using S and S_n (61 of 237, 26% of all clusters, for S and 34 of 237, 14% of all clusters, for S_n) as parameters for detection.

Obtained pictures were manually analyzed one by one with measured values of S and S_n. Figure 7 shows examples of single- and double-cell images having one, two, or three nuclei obtained from cancer-implanted and control blood, respectively. As shown in Fig. 7, the following 3 results were obtained: (i) single cells having multiple nuclei numbering more than two were specifically included in the cancer cell-implanted blood (count of 133, 3.2% of total single cells in cancer-implanted samples), (ii) two-cell clusters
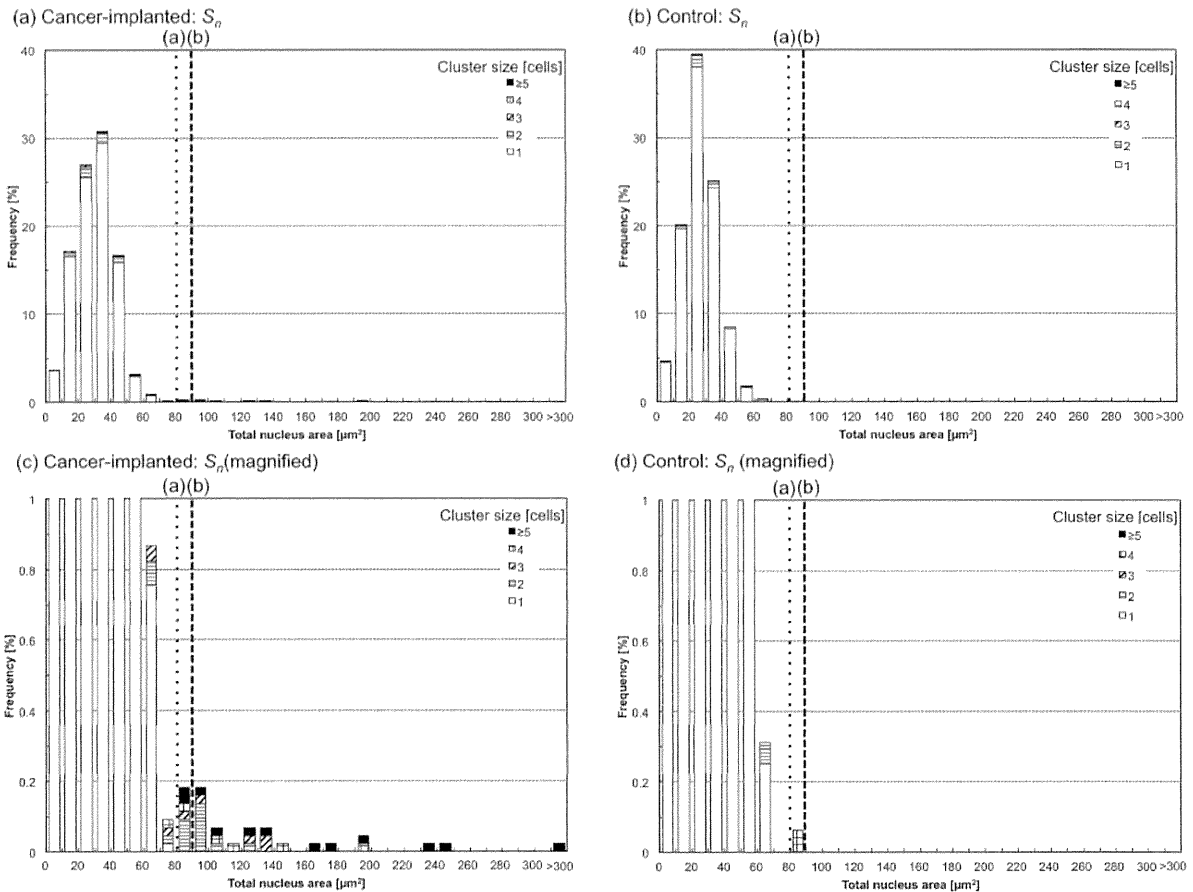
Figure 6. Histograms of total nucleus area, Sn, for cancer cell-implanted (a and c) and control blood (b and d). Two threshold values (a) and (b) for cluster identifications are indicated as dotted and dashed lines.
doi:10.1371/journal.pone.0104372.g006

having only one nucleus seemed to be single cells to which a small particle (possibly debris of a hemolyzed red cell) was attached (count of 126, 72% of total two-cell clusters in cancer-implanted samples and count of 41, 84% of total two-cell clusters in control), and (iii) two-cell clusters having two nuclei were either true clusters or two independent cells flowing alongside each other (count of 48, including 2 clusters having 3 nuclei caused by the inclusion of a cell with multiple nuclei, 28% of total two-cell clusters in cancer-implanted samples and count of 8, 16% of total two-cell clusters in control). The first of these results shows the potential for the detection of implanted cancer cells having multiple nuclei, and the second can be thought of as single cells in general. The third in principle makes it difficult to distinguish two-cell clusters from two single cells using pictures; therefore, such two-cell "clusters" were also contained in control blood.

Figure 8 shows typical clustered cells composed of more than 3 cells. As shown in the figure and also in Table 1, a few clusters composed of more than 3 cells were also detected in control blood (count of 7 in total), with the maximum cell number of 6. However, they seemed to be single or two independent cells to which small particles were attached (i.e., the same as result (ii) in Fig. 7), which could also be confirmed by the number of nuclei, N_n, in the cluster, which had a maximum of 2. On the other hand, clusters contained in cancer-implanted blood were composed of more than 3 cells, with 15 cells at maximum, which was also

confirmed by N_n in the cluster being more than 3. It is unlikely for more than 3 cells to be flowing alongside each other; therefore, we concluded that clusters composed of more than 3 cells containing more than 3 nuclei were truly clustered cells in the blood. Such large clusters were contained in cancer cell-implanted blood at a count of 33 (7 counts, 21% of 3-cell clusters, 12 counts, 75% of 4-cell clusters, 14 counts, 100% of $\geq$5-cell clusters, and 0.8% of the total). Measured values of N_n are summarized in Fig. 9 (a) (and also in Table 1). As shown in this figure, more than 99% of images in control blood had a single nucleus, and cell clusters having more than 3 nuclei were not contained in the blood. Figure 9 (b) also shows N_n summarized from the perspective of cluster size. As shown in the figure, large clusters in cancer-implanted blood had many nuclei, typically more than 3, indicating the possibility of the cluster formation of CTCs in the blood.

As shown in the above results, N_n is one useful imaging biomarker to identify cell clusters in blood; however, only using this marker for identification is insufficient because single cells having multiple nuclei were also contained in cancer cell-implanted blood, as shown in Fig. 7; therefore, we evaluated another imaging biomarker, perimeter ratio (R), for the identification of clustered cells. R is defined as the ratio between the actual perimeter obtained from the cell image and the perimeter calculated with a circle approximation of S. A low value of R indicates distorted conformation of the cell away from a circular

Table 1. Summary of total cell area, S, total nucleus area, S_n, number of nuclei, N_n, and perimeter ratio, R, for each cluster size.

Cancer-implanted (N = 4375)			Total cell area, S [μm^2]					Total nucleus area, S_n [μm^2]				
Cluster [cells]	Frequency [counts]	Frequency [%]	Average	Median	S.D.	Max.	Min.	Average	Median	S.D.	Max	Min
1	4138	94.58	62	62	15	133	11	30	31	12	73	7
2	174	3.98	88	75	33	194	36	36	33	19	122	10
3	33	0.75	133	124	58	263	53	45	33	35	134	12
4	16	0.37	219	208	57	393	136	74	52	46	195	24
≥5	14	0.32	515	421	180	1163	179	149	131	85	342	37
≥2	237	5.4	129	81	130	1163	36	47	35	41	342	10

Cancer-implanted (continued)			Number of nuclei, N_n					Perimeter ratio, R				
Cluster [cells]	Frequency [counts]	Frequency [%]	Average	Median	S.D.	Max.	Min.	Average	Median	S.D.	Max	Min
1	4138	94.58	1.03	1.00	0.20	3	1	0.96	0.96	0.02	1.00	0.90
2	174	3.98	1.30	1.00	0.50	3	1	0.89	0.91	0.05	0.97	0.76
3	33	0.75	1.82	2.00	0.88	4	1	0.83	0.82	0.06	0.95	0.67
4	16	0.37	2.75	3.00	1.13	4	1	0.84	0.84	0.07	0.95	0.74
≥5	14	0.32	5.00	5.00	1.15	10	2	0.80	0.80	0.03	0.89	0.79
≥2	237	5.4	1.70	1.00	1.26	10	1	0.87	0.89	0.06	0.97	0.67

Control (N = 1599)			Total cell area, S [μm^2]					Total nucleus area, S_n [μm^2]				
Cluster [cells]	Frequency [counts]	Frequency [%]	Average	Median	S.D.	Max.	Min.	Average	Median	S.D.	Max	Min
1	1543	96.50	48	44	16	121	11	27	26	10	69	7
2	49	3.06	99	83	36	169	40	28	28	12	61	7
3	3	0.19	119	127	62	177	54	23	24	10	32	13
4	2	0.13	187	187	14	197	177	51	51	43	81	20
≥5	2	0.13	116	116	24	133	99	32	44	18	57	32
≥2	56	3.5	104	88	39	197	40	29	28	14	81	7

Control (continued)			Number of nuclei, N_n					Perimeter ratio, R				
Cluster [cells]	Frequency [counts]	Frequency [%]	Average	Median	S.D.	Max.	Min.	Average	Median	S.D.	Max	Min
1	1543	96.50	1.00	1.00	0.00	1	1	0.96	0.96	0.02	1.00	0.90
2	49	3.06	1.16	1.00	0.37	2	1	0.82	0.84	0.05	0.91	0.70
3	3	0.19	1.67	2.00	0.58	2	1	0.83	0.83	0.06	0.89	0.77
4	2	0.13	1.50	1.50	0.71	2	1	0.81	0.81	0.08	0.86	0.75
≥5	2	0.13	1.00	1.00	0.00	1	1	0.81	0.81	0.01	0.82	0.80
≥2	56	3.5	1.20	1.00	0.40	2	1	0.82	0.83	0.05	0.91	0.70
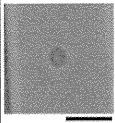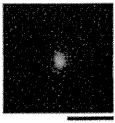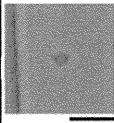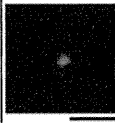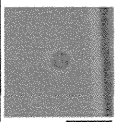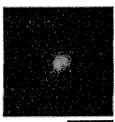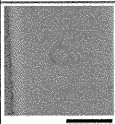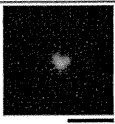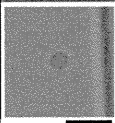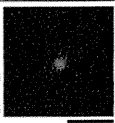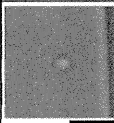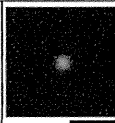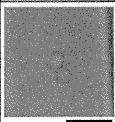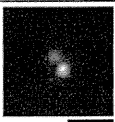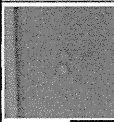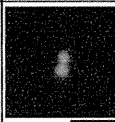
Cancer-implanted					Control				
Cluster size (N_n)	BF	FL	S [µm²]	S_n [µm²]	Cluster size (N_n)	BF	FL	S [µm²]	S_n [µm²]
1 (1) $n = 4005$			59	35	1 (1) $n = 1543$			55	21
1 (2) $n = 123$			57	41	1 (2)	N.A.			
1 (3) $n = 10$			72	47	1 (3)	N.A.			
2 (1) $n = 126$			67	26	2 (1) $n = 41$			69	40
2 (2) $n = 48$			117	74	2 (2) $n = 8$			73	61

Figure 7. Typical cell images for single and double cells in cancer cell-implanted and control blood. Each data count (*n*) indicates the image number having the same cluster size and N_n. Bars, 20 µm.

shape, which was expected for cell clusters. Figure 10 shows the relationship between the average value of R and cell cluster size for a cancer-implanted sample (detailed numbers are also shown in Table 1). As shown in the figure and table, all single cells had R higher than 0.90, with an average of 0.96, indicating that all cells having R smaller than 0.90 were clusters composed of more than 2 cells. On the other hand, R values for clusters composed of more than 2 cells were lower than 0.90 on average, and in detail, 131 clusters in cancer-implanted samples (55% of all clusters) and 55 clusters in control (98% of all clusters) had R lower than 0.90. Moreover, all large clusters composed of more than 3 cells having more than 3 nuclei, specifically observed only in cancer-implanted blood, had R lower than 0.90. These results indicate that more than half of the clusters, especially large clusters, could be identified by using R as an imaging biomarker.

According to the above results, large cluster formation of cancer cells in the blood was strongly expected. To confirm this, clusters larger than 300 µm² were collected by performing cell sorting in the chip, and their cell types were identified by measuring genome errors in the cells. Firstly, target genes that were included in the MAT-LyLu chromosome with abnormal copy numbers were searched by comparative genomic hybridization (CGH) assay using the cell line, with liver tissue of the rat as a reference. Two particularly abundant genes, *csrp2* and *zdhhc17* located on chromosome 7q13, were found (Fig. 11 (a)) and set as target genes for the identification of cancer cells in the blood. Next, the TaqMan copy number assay was performed for cells collected in

both the collection reservoir and the discarded reservoir (see Fig. 3). From the results, increases of copy numbers for both *csrp2* and *zdhhc17* were specifically observed for clustered cells collected in the collection reservoir (Fig. 11 (b)). These results indicate that large clusters, which were specifically observed in cancer cell-implanted blood, were CTCs.

Discussion

In this study, four imaging biomarkers, cell area, nucleus area, number of nuclei, and perimeter ratio (S, S_n, N_n, and R),were evaluated for the identification of cell clusters in the blood. From the results, some threshold values were obtained for each imaging biomarker, namely, (1) S larger than 200 µm² and (2) S_n larger than 90 µm² were specific to cancer cell-implanted blood. In addition, (3) N_n higher than 3 was also specific to cancer cell-implanted blood. Finally, (4) all clustered cells composed of more than 3 cells having N_n higher than 3, which was specific to cancer cell-implanted blood, had R lower than 0.90. According to these results, the use of R is one useful approach for the identification of clustered cells having multiple nuclei numbering more than 3, which are specific to cancer cell-implanted blood. S and S_n are also useful parameters for the identification of extremely large clusters, which are quite likely to be CTCs. For small clusters composed of two cells, it is in principle difficult to distinguish whether the cluster is an actual cluster or two independent cells flowing alongside each other by using image-based analysis. One potential approach to distinguish these possibilities is the

Cancer-implanted					Control				
Cluster size (N_n)	BF	FL	S [μm^2]	S_n [μm^2]	Cluster size (N_n)	BF	FL	S [μm^2]	S_n [μm^2]
3 (3) $n = 6$			251	126	3 (1) $n = 1$			53	12
4 (4) $n = 4$			258	147	4 (1) $n = 1$			197	20
6 (6) $n = 1$			388	179	5 (1) $n = 1$			99	32
15 (max., 10) $n = 1$			1163	342	6 (max., 1) $n = 1$			133	50

Figure 8. Typical cell images for clustered cells composed of more than three cells in cancer cell-implanted and control blood. Each data count (n) indicates the image number having the same cluster size and N_n. Bars, 20 μm.
doi:10.1371/journal.pone.0104372.g008

combination of the image-based analysis suggested in this study with a molecular analytical approach, such as quantitative gene copy number assays of the targeted cells. The system developed in this study has been combined with a cell sorting unit and can perform the combination measurement of multi-imaging analysis with molecular analysis, as shown in Fig. 11, which indicates the advantage of our developed system.

For the detection of CTCs, some methods were suggested. The principles were in general separated into two kinds; one was based on the chemical reaction and the other was physical detection. The former is in general based on the labeling of target molecules on the CTCs with antibodies, and it was sometimes combined with microfabrication technologies to improve detection sensitivities [6,7]. However, this approach sometimes yielded false-negative detection because of the variety of molecular expression levels in
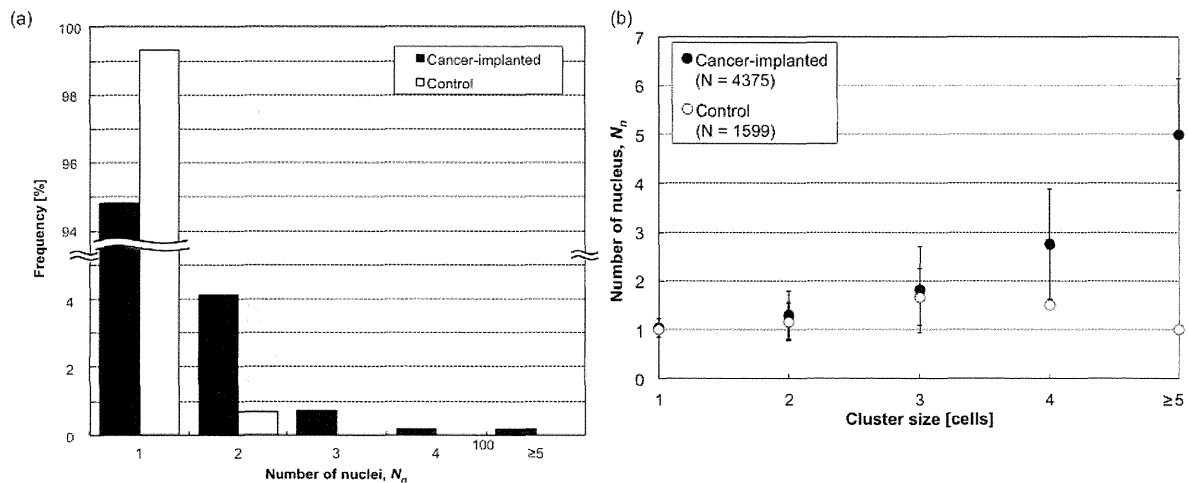

Figure 9. Summary of the number of nuclei, N_n. (a) A histogram of N_n obtained from cancer cell-implanted and control blood. (b) The relationship between N_n and cell cluster size.
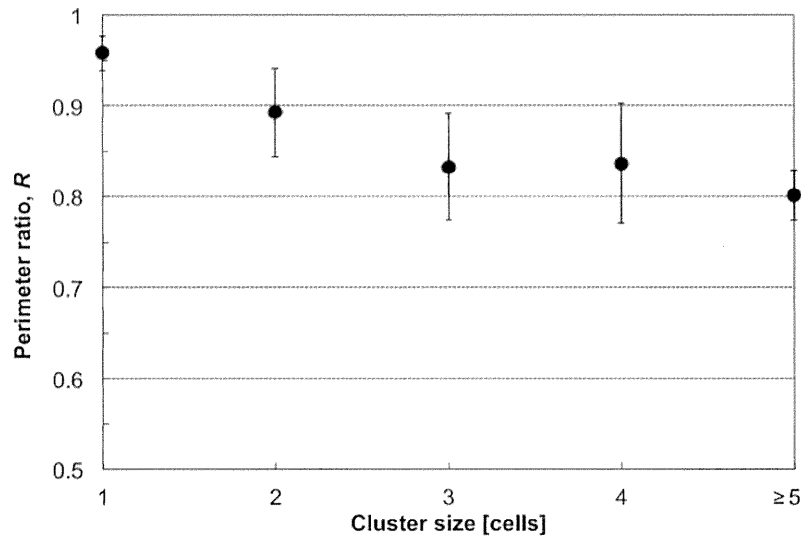doi:10.1371/journal.pone.0104372.g009

Figure 10. The relationship between perimeter ratio, R, and cell cluster size obtained from cancer cell-implanted blood.
doi:10.1371/journal.pone.0104372.g010

CTCs. For this latter case, various physical parameters of CTCs such as cell diameter [4,16,17] and dielectrophoretic properties [5] have been used with a combination of microfabrication technologies. According to the results in this study, cell size (S) is one useful parameter to find irregular cells in blood samples such as clustered cells; however, the use of only one parameter is insufficient for the exhaustive detection of CTCs. Our developed system can use various parameters including both chemical and physical properties to find target cells, which would also be useful for the detection of various CTCs.
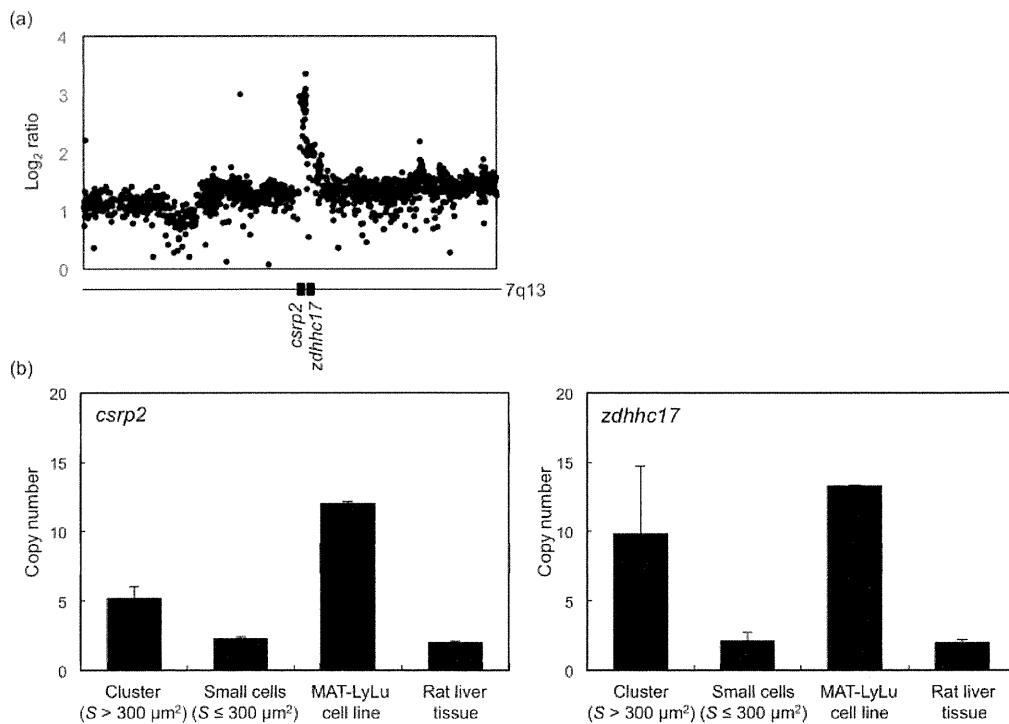
Figure 11. Results of quantitative gene copy number assays. (a) Results of CGH assays performed for the MAT-LyLu cell line. Liver tissue of the rat was used as a reference. Gene amplifications for *csrp2* and *zdhhc17* located on chromosome 7q13 were found. (b) Results of TaqMan copy number assays performed with clusters larger than 300 μm^2 collected in the collection reservoir, and cells smaller than 300 μm^2 collected in the discarded reservoir. Results of the assays for the MAT-LyLu cell line (positive control) and liver tissue (negative control) are also shown.
doi:10.1371/journal.pone.0104372.g011

In this study, large clusters were specifically observed in cancer cell-implanted blood, and an approach for finding these clusters in the blood has possibility for the development of a new cancer metastasis diagnostic method. Results in this study were obtained using hemolyzed blood samples *in vitro*; therefore, the large cluster formations should also be confirmed for blood *in vivo* as a next step to achieve such a new diagnostic method. One possibility for the mechanism of large cluster formation is an aggregation of implanted cancer cells by immune reaction of the rat with antibody formation. In this study, blood samples were picked up from the rat 2 weeks after implantation; therefore, time-course measurements of cluster formations after implantation might be one useful way to confirm the above possibility, and our developed system can also be used to confirm this.

Conclusion

In this study, an on-chip multi-imaging flow cytometry system was developed to find cell clusters in blood samples. The system can take both BF and FL pictures simultaneously, and can obtain imaging biomarkers; cell area, nucleus area, number of nuclei, and perimeter ratio (S, S_n, N_n, and R), in real time. By using the developed system, sample blood of rats in which cancer cells had been pre-implanted was measured and compared with that of

healthy rats. In terms of the results, clustered cells having (1) S larger than 200 μm^2 and (2) S_n larger than 90 μm^2 were specifically observed in cancer cell-implanted blood, but were not observed in healthy rats. In addition, (3) N_n higher than 3 was specific for cancer-implanted blood and (4) R smaller than 0.90 was specific for all clusters having N_n higher than 3, which were specific for cancer-implanted blood. Finally, quantitative gene copy number assay was performed for the large clusters, and they were shown to be CTCs. These results indicate the usefulness of the imaging biomarkers for characterizing clusters, and that the developed system is useful to identify clustered CTCs in blood.

Acknowledgments

Author Contributions

Conceived and designed the experiments: HK TA KN YM KY. Performed the experiments: HK HT YN KS AH MO MG TA. Analyzed the data: HK KS AH MO MG TA KN YM KY. Contributed reagents/materials/analysis tools: HK HT YN KS AH MO MG TA KN YM KY. Wrote the paper: HK KY.

References

1. Cristofanilli M, Budd GT, Ellis MJ, Stopeck A, Matera J, et al. (2004) Circulating tumor cells, disease progression, and survival in metastatic breast cancer. N Engl J Med 351: 781–791.
2. Sethi N, Kang Y (2011) Unravelling the complexity of metastasis - molecular understanding and targeted therapies. Nat Rev Cancer 11: 735–748.
3. Yu M, Stott S, Toner M, Maheswaran S, Haber DA (2011) Circulating tumor cells: approaches to isolation and characterization. J Cell Biol 192: 373–382.
4. Davis JA, Inglis DW, Morton KJ, Lawrence DA, Huang LR, et al. (2006) Deterministic hydrodynamics: taking blood apart. Proc Natl Acad Sci U S A 103: 14779–14784.
5. Gascoyne PR, Noshari J, Anderson TJ, Becker FF (2009) Isolation of rare cells from cell mixtures by dielectrophoresis. Electrophoresis 30: 1388–1398.
6. Nagrath S, Sequist LV, Maheswaran S, Bell DW, Irimia D, et al. (2007) Isolation of rare circulating tumour cells in cancer patients by microchip technology. Nature 450: 1235–1239.
7. Stott SL, Hsu CH, Tsukrov DI, Yu M, Miyamoto DT, et al. (2010) Isolation of circulating tumor cells using a microvortex-generating herringbone-chip. Proc Natl Acad Sci U S A 107: 18392–18397.
8. Zheng S, Lin HK, Lu B, Williams A, Datar R, et al. (2011) 3D microfilter device for viable circulating tumor cell (CTC) enrichment from blood. Biomed Microdevices 13: 203–213.
9. Budd GT, Cristofanilli M, Ellis MJ, Stopeck A, Borden E, et al. (2006) Circulating tumor cells versus imaging–predicting overall survival in metastatic breast cancer. Clin Cancer Res 12: 6403–6409.
10. Danila DC, Heller G, Gignac GA, Gonzalez-Espinoza R, Anand A, et al. (2007) Circulating tumor cell number and prognosis in progressive castration-resistant prostate cancer. Clin Cancer Res 13: 7053–7058.
11. Takahashi K, Hattori A, Suzuki I, Ichiki T, Yasuda K (2004) Non-destructive on-chip cell sorting system with real-time microscopic image processing. J Nanobiotechnology 2: 5.
12. Hayashi M, Hattori A, Kim H, Terazono H, Kaneko T, et al. (2011) Fully automated on-chip imaging flow cytometry system with disposable contamination-free plastic re-cultivation chip. Int J Mol Sci 12: 3618–3634.
13. Yasuda K, Hattori A, Kim H, Terazono H, Odaka M, M G, et al. (2013) Non-destructive on-chip imaging flow cell-sorting system for on-chip cellomics. Microfluidics and Nanofluidics 14: 907–931.
14. Vona G, Sabile A, Louha M, Sitruk V, Romana S, et al. (2000) Isolation by size of epithelial tumor cells - A new method for the immunomorphological and molecular characterization of circulating tumor cells. American Journal of Pathology 156: 57–63.
15. Desitter I, Guerrouahen BS, Benali-Furet N, Wechsler J, Janne PA, et al. (2011) A New Device for Rapid Isolation by Size and Characterization of Rare Circulating Tumor Cells. Anticancer Research 31: 427–441.
16. Hosokawa M, Kenmotsu H, Koh Y, Yoshino T, Yoshikawa T, et al. (2013) Size-Based Isolation of Circulating Tumor Cells in Lung Cancer Patients Using a Microcavity Array System. Plos One 8.
17. Hosokawa M, Yoshikawa T, Negishi R, Yoshino T, Koh Y, et al. (2013) Microcavity Array System for Size-Based Enrichment of Circulating Tumor Cells from the Blood of Patients with Small-Cell Lung Cancer. Analytical Chemistry 85: 5692–5698.
18. Abdalla F, Boder J, Markus R, Hashmi H, Buhmeida A, et al. (2009) Correlation of nuclear morphometry of breast cancer in histological sections with clinicopathological features and prognosis. Anticancer Res 29: 1771–1776.
19. Buhmeida A, Algars A, Ristamaki R, Collan Y, Syrjanen K, et al. (2006) Nuclear size as prognostic determinant in stage II and stage III colorectal adenocarcinoma. Anticancer Res 26: 455–462.
20. de Andrea CE, Petrilli AS, Jesus-Garcia R, Bleggi-Torres LF, Alves MT (2011) Large and round tumor nuclei in osteosarcoma: good clinical outcome. Int J Clin Exp Pathol 4: 169–174.
21. Deans GT, Hamilton PW, Watt PC, Heatley M, Williamson K, et al. (1993) Morphometric analysis of colorectal cancer. Dis Colon Rectum 36: 450 456.
22. Dundas SA, Laing RW, O'Cathain A, Seddon I, Slater DN, et al. (1988) Feasibility of new prognostic classification for rectal cancer. J Clin Pathol 41: 1273–1276.
23. Meachem MD, Burgess HJ, Davies JL, Kidney BA (2012) Utility of nuclear morphometry in the cytologic evaluation of canine cutaneous soft tissue sarcomas. J Vet Diagn Invest 24: 525–530.
24. Sokmen S, Sarioglu S, Fuzun M, Terzi C, Kupelioglu A, et al. (2001) Prognostic significance of angiogenesis in rectal cancer: a morphometric investigation. Anticancer Res 21: 4341–4348.
25. Tennant TR, Kim H, Sokoloff M, Rinker-Schaeffer CW (2000) The Dunning model. Prostate 43: 295–302.
26. Hattori A, Yasuda K (2010) Comprehensive Study of Microgel Electrode for On-Chip Electrophoretic Cell Sorting. Japanese Journal of Applied Physics 49: 06GM04.
27. Hattori A, Kim H, Terazono H, Odaka M, M G, et al. (2014) Identification of cells using morphological information of bright field/fluorescent multi-imaging flow cytometer images. Japanese Journal of Applied Physics, in press.
28. Kinosita K, Jr., Itoh H, Ishiwata S, Hirano K, Nishizaka T, et al. (1991) Dual-view microscopy with a single camera: real-time imaging of molecular orientations and calcium. J Cell Biol 115: 67–73.
29. Nomura F, Kaneko T, Hattori A, Yasuda K (2011) Label-Free Shape-Based Selection of Cardiomyocytes with on-Chip Imaging Cell Sorting System. J Bioproces Biotechniq S3:003.

Clinical Cancer Research

AACR

Tyrosine Phosphoproteomics Identifies Both Codrivers and Cotargeting Strategies for T790M-Related EGFR-TKI Resistance in Non–Small Cell Lung Cancer

Takeshi Yoshida, Guolin Zhang, Matthew A. Smith, et al.

Updated version	Access the most recent version of this article at: doi:10.1158/1078-0432.CCR-13-1559
Supplementary Material	Access the most recent supplemental material at: http://clincancerres.aacrjournals.org/content/suppl/2014/06/16/1078-0432.CCR-13-1559.DC1.html

Cited Articles	This article cites by 48 articles, 25 of which you can access for free at: http://clincancerres.aacrjournals.org/content/20/15/4059.full.html#ref-list-1

E-mail alerts	Sign up to receive free email-alerts related to this article or journal.
Reprints and Subscriptions	To order reprints of this article or to subscribe to the journal, contact the AACR Publications Department at pubs@aacr.org.
Permissions	To request permission to re-use all or part of this article, contact the AACR Publications Department at permissions@aacr.org.

**Clinical
Cancer
Research**

Cancer Therapy: Preclinical

Tyrosine Phosphoproteomics Identifies Both Codrivers and Cotargeting Strategies for T790M-Related EGFR-TKI Resistance in Non–Small Cell Lung Cancer

Takeshi Yoshida[1,5], Guolin Zhang[1], Matthew A. Smith[1], Alex S. Lopez[2], Yun Bai[1], Jiannong Li[1], Bin Fang[3], John Koomen[3], Bhupendra Rawal[4], Kate J. Fisher[4], Ann Y. Chen[4], Michiko Kitano[5], Yume Morita[5], Haruka Yamaguchi[5], Kiyoko Shibata[5], Takafumi Okabe[5], Isamu Okamoto[5], Kazuhiko Nakagawa[5], and Eric B. Haura[1]

Abstract

Purpose: Irreversible EGFR-tyrosine kinase inhibitors (TKI) are thought to be one strategy to overcome EGFR-TKI resistance induced by T790M gatekeeper mutations in non–small cell lung cancer (NSCLC), yet they display limited clinical efficacy. We hypothesized that additional resistance mechanisms that cooperate with T790M could be identified by profiling tyrosine phosphorylation in NSCLC cells with acquired resistance to reversible EGFR-TKI and harboring T790M.

Experimental Design: We profiled PC9 cells with TKI-sensitive *EGFR* mutation and paired EGFR-TKI–resistant PC9GR (gefitinib-resistant) cells with T790M using immunoaffinity purification of tyrosine-phosphorylated peptides and mass spectrometry–based identification/quantification. Profiles of erlotinib perturbations were examined.

Results: We observed a large fraction of the tyrosine phosphoproteome was more abundant in PC9- and PC9GR-erlotinib–treated cells, including phosphopeptides corresponding to MET, IGF, and AXL signaling. Activation of these receptor tyrosine kinases by growth factors could protect PC9GR cells against the irreversible EGFR-TKI afatinib. We identified a Src family kinase (SFK) network as EGFR-independent and confirmed that neither erlotinib nor afatinib affected Src phosphorylation at the activation site. The SFK inhibitor dasatinib plus afatinib abolished Src phosphorylation and completely suppressed downstream phosphorylated Akt and Erk. Dasatinib further enhanced antitumor activity of afatinib or T790M-selective EGFR-TKI (WZ4006) in proliferation and apoptosis assays in multiple NSCLC cell lines with T790M-mediated resistance. This translated into tumor regression in PC9GR xenograft studies with combined afatinib and dasatinib.

Conclusions: Our results identified both codrivers of resistance along with T790M and support further studies of irreversible or T790M-selective EGFR inhibitors combined with dasatinib in patients with NSCLC with acquired T790M. *Clin Cancer Res; 20(15); 4059–74. ©2014 AACR.*

Introduction

Despite the benefits shown with EGFR-tyrosine kinase inhibitor (EGFR-TKI) treatment in patients with non–small

Authors' Affiliations: [1]Department of Thoracic Oncology, [2]Tissue Core, [3]Proteomics and Molecular Oncology Program, [4]Biostatistics Program, H. Lee Moffitt Cancer Center and Research Institute, Tampa, Florida; and [5]Department of Medical Oncology, Kinki University Faculty of Medicine, Osaka-Sayama, Osaka, Japan

T. Yoshida and G. Zhang contributed equally to this article.

Corresponding Author: Eric B. Haura, Department of Thoracic Oncology, H. Lee Moffitt Cancer Center and Research Institute, 12902 Magnolia Drive, Tampa, FL 33612. Phone: 181-3745-6827; Fax: 181-3745-6817; E-mail: eric.haura@moffitt.org

cell lung cancer (NSCLC) with TKI-sensitive *EGFR* mutations (1, 2), acquired resistance is a critical clinical problem. A secondary point mutation in exon 20 of *EGFR* that substitutes methionine for threonine at amino acid position 790 (T790M) was identified in patients with NSCLC who developed acquired resistance to gefitinib or erlotinib (3, 4). Nearly 50% of patients with NSCLC with acquired resistance to EGFR-TKIs have the T790M secondary mutation (5–7). Irreversible EGFR-TKIs, such as CL387,785 (8), PF00299804 (9), BIBW-2992 (afatinib; ref. 10), and HKI-272 (11), are thought to be one strategy to overcome T790M-induced resistance. However, a number of studies have shown their limited activity in cells with T790M mutations given the increased affinity of ATP binding to T790M EGFR proteins or through mechanisms affecting other pathways such as MET activation (8, 9, 12–18). Clinical studies have also highlighted the limited efficacy of irreversible EGFR-TKIs. In the LUX-Lung 1 Trial,

Translational Relevance

Acquired resistance to EGFR-tyrosine kinase inhibitor (EGFR-TKI) is a critical clinical problem in patients with non–small cell lung cancer (NSCLC) with TKI-sensitive EGFR mutation. We applied mass spectrometry–based tyrosine phosphoproteomics to paired TKI-sensitive and resistant cell lines to visualize molecular networks related to the acquired EGFR-TKI resistance. The results suggest that multiple receptors and signaling molecules such as MET, AXL, and IRS2 can collaborate to drive resistance to EGFR-TKI. We also identified Src family kinases (SFK) as a central signaling hub in TKI-resistant cells with T790M gatekeeper mutation. SFK phosphorylation was also detected in human NSCLC samples with T790M. In vitro and in vivo experiments demonstrated that irreversible EGFR-TKI (afatinib) or T790M-selective EGFR-TKI (WZ4006) combined with the SFK inhibitor dasatinib overcame T790M-mediated resistance, thereby nominating a new strategy for translation into the clinic.

conducted to compare afatinib treatment versus placebo in patients with advanced NSCLC whose disease progressed after receiving first-generation EGFR-TKIs (erlotinib, gefitinib), afatinib did not extend the primary endpoint of overall survival despite significant improvements in progression-free survival (19). These preclinical and clinical results suggest that irreversible EGFR-TKIs as single agents are insufficient to overcome resistance.

One strategy to improve on the limited efficacy of irreversible EGFR-TKI is through combination with other pathway inhibitors. For example, studies that combined afatinib with the anti-EGFR monoclonal antibody cetuximab (20) or the PI3K/mTOR inhibitor PI-103 (12) and HKI-272 combined with mTOR inhibitor rapamycin (21) have shown promise in overcoming T790M resistance. Another reason for the limited efficacy of agents targeting T790M could be mediated through other tyrosine kinases, such as receptor tyrosine kinases (RTK), which provide additional protection against EGFR-TKIs (22). Recent studies have shown that growth factor ligands can protect oncogene-addicted cells from molecularly targeted agents; thus, altered expression of these growth factor receptors could further identify resistance pathways (23–25).

We explored the underlying ability of some growth factor ligands to drive resistance to TKIs by examining the basal tyrosine phosphoproteome and the effects of EGFR-TKIs on other RTKs. In this study, we tested the hypothesis that a global evaluation of tyrosine phosphorylation (using mass spectrometry) between the sensitive and resistant cells, along with EGFR perturbations, could identify additional resistance mechanisms that could give insight into cotargeting strategies. Our results identified numerous coexpressed RTKs and non-RTKs that, under proper environmental circumstances, cooperate to drive resistance to EGFR-TKIs. We further showed that Src family kinase (SFK) signaling

was independent of EGFR signaling and that cotargeting SFKs with afatinib led to combined growth suppression in *in vitro* and *in vivo* in cells with T790M. Globally, our results suggest that an unbiased mass spectrometry approach can identify codrivers of resistance that can be cotargeted to enhance efficacy of targeted agents.

Materials and Methods

Reagents

Gefitinib, erlotinib, afatinib, and WZ4002 were purchased from Chemie Tek (Indianapolis, IN). CL-387,785 was purchased from AXXORA (San Diego, CA).

Cell culture

The human H1975, H460, A549, and H1299 NSCLC cell lines were obtained from American Type Culture Collection. The human HCC4006 NSCLC cells were kindly provided by Dr. Paul Bunn (University of Colorado, Aurora, CO). The human HCC827 NSCLC cells were provided by Dr. Jon Kurie (MD Anderson Cancer Center, Houston, TX). The human PC9 NSCLC cell line was kindly provided by Dr. Hayata, Tokyo Medical University (Tokyo, Japan). PC9GR cells were generated by exposure of PC9 cells containing a TKI-sensitive EGFR mutation (exon 19; E746-A750) to gradually increasing concentrations of gefitinib, beginning at 3 nM and up to 2 μM, for 3 months. HCC4006-T790M and HCC827-T790M cells were generated as previously described (26). All cell lines have been maintained in a central repository at Moffitt since 2008. All cell lines had been authenticated by STR analysis (ACTG Inc, Wheeling, IL) as of September 2010, and all cells had been routinely tested and were negative for mycoplasma (PlasmoTest, InvivoGen, San Diego, CA). Cell viability was determined using the CellTiter-Glo® Luminescent Cell Viability Assay (Promega, Madison, WI). Apoptosis assays were performed using PE-conjugated monoclonal active caspase-3 antibody apoptosis kit (BD Biosciences). Rescue experiments were done as previously described (27).

Genotyping

Total genomic DNA from parental and resistant cells was prepared using the DNeasy Blood & Tissue Kit (Qiagen, Valencia, CA) in accordance with the product manual. Direct DNA sequencing was used to detect EGFR mutations as previously described (28). We also applied the PCR-invader assay to detect minor populations of EGFR mutation, as previously described (29). MET gene copy number per cell was determined by fluorescence in situ hybridization with the use of the LSI D7S522 (7q31) Spectrum Orange and chromosome 7 centromere (CEP7) Spectrum Green probes (Vysis; Abbott), as previously described (30).

Tyrosine phosphoproteomics

Tyrosine phosphopeptides were purified according to the manufacturer's recommendations for the Cell Signaling PhosphoScan kit (P-Tyr-100) (Cell Signaling Technology). Briefly, 2 × 108 cells were lysed in urea buffer; extracted

proteins (40–80 mg) were then reduced by dithiothreitol, alkylated by iodoacetamide, and then digested by trypsin. Peptide mixture was isolated from lysate using Sep-Pak C18 columns and then lyophilizated. Phosphorylated peptides were immunoaffinity purified using phosphotyrosine antibody after lyophilizated peptide mixture was dissolved. Volumes of phosphotyrosine peptides were then downsized to 20 μL by vacuum drying for further experiments. The further peptide mixture separation and phosphosite assigning have been previously described (31). To quantify each tyrosine-contained peptide, we calculated peak area [also called extraction ion chromatography (EIC)] using Label-free strategy and xCalibur as the tools. Identification and quantification of some obscure peptides were manually verified. After quantification, 774 phosphorylated tyrosine sites were identified. An in-house algorithm was implemented to identify unique phosphorylation tyrosine (pY) sites, remove redundant sites, and merge miss-cleaved peptides by using protein ID, peptide sequence, and phosphorylation start-site index, with quantification of peak areas. When only identifiable to the level of pairs of pYs (e.g., next to each other or up to ~11 amino acids apart), then the independent unit for analysis was the unique pY pair (instead of single site). Mis-cleaved phosphopeptides or fragments of the same phosphopeptides were merged. Peptides shared by multiple proteins were annotated. Among which, two pairs of sequences were potential results of co-elution and therefore not included in further analyses. A total of 524 unique phosphotyrosine units (pYs) or pY pairs were identified. Quantification and stability of 5 MYG peptides across samples were examined, with the average of 3 of them used for normalizing the peak ratio areas across 16 samples (8 biological samples with technical duplicates) so that the normalized quantities across samples were comparable. Reproducibility between technical replicates for each pY was estimated using Pearson correlation. The corresponding P values were used to estimate false discovery rate. High technical reproducibility of FDR ≤1% was used in our study. In addition, if the pY was detected in at least half of the samples in this study, i.e., at least 8 of 16 samples, it passed the QC criteria. Among the 524 unique pY units, 403 of them passed the QC criteria and were included in the analyses. 377 of them were unique pY sites while 26 of them were unique pY pairs. Averages of technical replicates from 8 biological samples were used in the analyses. We used a simple imputation (i.e., when one of technical replicates is missing, the detected value from the other remaining technical replicate was used). Data were analyzed in log2 scale prior to parametric analyses and also for ease of interpretation. For example, the difference of 1 in log2 scale is a 2-fold change between two conditions. Two-way ANOVA with the interaction term was performed to answer the following three research questions: 1) Which tyrosine sites are differentially phosphorylated between the cell lines with and without drug resistance? 2) Which tyrosine sites are differentially phosphorylated between the control and erlotinib-treated groups? 3) Which pYs phosphorylation response to treatment is different between the resistant and non-resistant cell line? To adjust for multiple hypothesis testing, the resulting P values for the main effects of cell line and treatment as well as the cell line-by-treatment interaction term were used to estimate false discovery rate. We used FDR ≤20% to declare statistical significance. We further performed network analysis based on these potential candidates. Interactions among all identified tyrosine phosphorylated proteins were retrieved from the Molecular Interaction database (MINT) (32); the IntAct database (33); the Database of Interacting Proteins (DIP) (34); the General Repository for Interaction Datasets (BioGRID) (35) and the Biomolecular Interaction Network Database (BIND) (36) using InnateDB (37) and visualized in Cytoscape 2.8.3 (38).

Protein expression analysis

Western blot analysis of whole cell lysates was performed as described previously (27). Primary antibodies to EGFR, MET, pTyr 1234/1235 MET, IRS2, pTyr 1131 IGF1R, AXL, pTyr 702 AXL, Src, pTyr 416 Src, Akt, pSer 473 Akt, Erk, pThr202/Tyr204 Erk, and PARP were obtained from Cell Signaling Technology. Primary antibodies to pY1068-EGFR were obtained from Invitrogen (Carlsbad, CA). Primary antibodies to β-actin were purchased from Sigma-Aldrich (St. Louis, MO).

Assessment of tumor growth inhibition *in vivo*

All animal procedures were approved by our Institutional Animal Care and Use Committee. PC9GR cells (2×106) were injected subcutaneously into the flank of 7-week-old female athymic nude mice. The mice were divided into 4 treatment groups of 7 animals: those treated over 3 weeks by daily oral gavage of vehicle, afatinib (10 mg/kg), dasatinib (15 mg/kg), or both afatinib and dasatinib; 0.5% (wt/vol) aqueous solution of hydroxypropylmethylcellulose was used as vehicle for afatinib, and 50% propylene glycol was used as vehicle for dasatinib. Treatment was initiated when tumors in each group achieved an average volume of 100 mm³, with tumor volume being determined twice weekly for 21 days after the onset of treatment from caliper measurement of tumor length (L) and width (W) according to the formula LW2/2.

Src-Tyr416 immunohistochemistry staining

Immunohistochemistry staining was performed to measure the expression of phosphor-Src (Tyr416) in paraffin tissues from 10 lung cancer patients with mutant-positive EGFR T790M.

Slides were stained for phosphor-Src (Tyr416) (mouse monoclonal antibody; Millipore) using a Ventana Discovery XT automated system (Ventana Medical Systems, Tucson, AZ) following the manufacturer's protocol with proprietary reagents. Briefly, slides were deparaffinized on the automated system with EZ Prep solution (Ventana). Enzymatic retrieval method was used in protease 1 at 4 minute (Ventana), CC1 Standard and CC2 standard conditions. The primary monoclonal antibody (Millipore) reacts to secondary antibody at different dilution-titrations. Both primary and secondary

antibodies were incubated following Ventana's instruction and the antibody product recommendation. The intensity of phosphor-Src expression was scored from 0–3 (0 = no expression, 1 = weak expression, 2 = moderate expression, and 3 = high expression), while the cellularity was scored from 0–3 (0 = 0%, 1 = 1-33%, 2 = 34-66%, and 3 = >66%). The H scores formed by intensity of immunoactivity timing cellularity were stratified as low (0–2), intermediate (3–4), and high (6–9).

MET-pY100 proximity ligation and total MET immunofluorescence

Slides containing 5-μm sections were rehydrated through xylene and graded alcohols. Heat-induced epitope retrieval was carried out in Tris-EDTA (pH 9) in a pressure cooker for 20 minutes and then allowed to cool for 20 minutes. Nonspecific binding was blocked by incubation with 1.5% BSA, and primary antibodies were incubated overnight in 1.5% BSA-PBST.

For proximity ligation, antibodies were rabbit anti-MET (clone D1C2, Cell Signaling Technology) and mouse ant-pY100 (Cell Signaling Technology). PLA probes were anti-rabbit (-) and anti-mouse (+) and were incubated for 1 hour in 0.15% BSA/PBST. Detection was carried out using the DuoLink in situ PLA Far Red kit (O-Link Biosciences, Uppsala, Sweden). AlexaFluor 488-conjugated anti-cyto-keratin was used to demarcate epithelial regions (clone AE1/AE3, eBiosciences).

For immunofluorescence, antibodies were rabbit anti-MET (clone D1C2, Cell Signaling Technology) and detected via AlexaFluor 647-labeled anti-rabbit secondary antibodies (Invitrogen). Murine pan-cytokeratin (clone AE1/AE3, Dako) was used to demarcate epithelial regions (tumor mask) and detected via AlexaFluor 555-labeled anti-mouse secondary antibodies (Invitrogen). Images were acquired on a PM2000.

Statistical methods

Anderson-Darling statistics and normal curves were examined to assess whether tumor measurements were normally distributed. A square-root transformation was performed on the tumor measurements to make them approximately normal. ANOVA test was used to assess whether there was a statistically significant difference on tumor sizes measured across treatment groups at each time point. Tukey-Kramer method was used to perform all pairwise group comparisons. All statistical analyses were performed using SAS (version 9.2; SAS Institute; Cary, NC).

Results

Chronic gefitinib exposure of PC9 cells generates stable cell-autonomous resistance to EGFR-TKIs with T790M

After generation of PC9GR cells, we identified single-cell clones of PC9GR cells that were highly resistant to erlotinib (Supplementary Fig. S1A). Although PC9GR cells are partially sensitive to the irreversible EGFR-TKI CL387,785 as expected from a previous report (8), IC_{50} for CL387,785 was

100-fold increased compared with parent PC9 cells (Supplementary Fig. S1A). This resistance was stable as it was not reversed by culturing PC9GR cells for up to 6 months in gefitinib-free medium (data not shown). PC9GR cells acquired T790M while retaining exon 19 E746-A750, as determined by both direct DNA sequencing and PCR-invader assay (Supplementary Fig. S2A). In addition, we did not find MET amplification by FISH analysis in PC9GR cells (Supplementary Fig. S2B), which is another mechanism of acquired EGFR-TKI resistance in NSCLC (28). Erlotinib still has partial inhibitory effects on EGFR phosphorylation in PC9GR cells (Supplementary Fig. S1B), consistent with prior studies that T790M typically emerges as a minor population and resistant cells retain drug-sensitive alleles (8, 33). However, erlotinib could not completely inhibit downstream pAkt and pErk in PC9GR cells, consistent with resistance to EGFR-TKIs in the presence of T790M (Supplementary Fig. S1B).

System-level comparison of tyrosine phosphorylation identifies common RTK pathways associated with erlotinib resistance

We hypothesized that erlotinib-resistant PC9GR cells could collect additional mechanisms of resistance through acquired alterations in tyrosine kinase signaling that could collaborate with T790M to codrive resistance to EGFR-TKI. We therefore profiled tyrosine kinase signaling by charting tyrosine phosphorylated peptides in PC9 and PC9GR cells. As shown in our schema (Fig. 1), tryptic peptides were derived from cellular protein lysates and enriched with anti-phosphotyrosine (pTyr) antibodies followed by identification and quantification using liquid chromatography coupled with tandem mass spectrometry (LC/MS-MS; refs. 32, 34). Changes in peptides in PC9GR cells were identified and compared with PC9 cells, thus allowing us to determine additional changes beyond T790M that could be codrivers of TKI resistance. We perturbed EGFR-driven signaling in erlotinib-sensitive PC9 and erlotinib-resistant PC9GR cells to identify EGFR-dependent pathways/networks and potential pathways/networks independent of EGFR signaling that could play a role in EGFR-TKI resistance. After 1-hour erlotinib treatment, cell pellets were collected and pTyr peptides were identified in untreated and treated PC9 and PC9GR cells. Changes in peptides were identified compared with control vehicle-treated cells in each of the two cell lines. We hypothesized that this approach would identify downstream signaling events driven by mutated EGFR but could also potentially identify proteins or pathways activated by TKI or unaltered by TKI that could, under the correct circumstances, potentiate drug resistance. In total, between the two cell lines, we identified 403 pTyr peptides corresponding to 265 unique phosphoproteins. Examples of extracted ion chromatograms for pTyr peptides corresponding to EGFR and MET are shown in Supplementary Figs. S3 and S4.

We next compared changes in pTyr abundance between PC9 and PC9GR cells (Fig. 2A; Supplementary Table S1). We found 110 unique pTyr peptides (76 proteins) that were

Figure 1. Phosphoprotein network associated with mutant EGFR and T790M tyrosine kinase signaling. Workflow of quantitative phosphoproteomics analysis. EIC, extracted ion chromatography (used to quantify peptide abundance for each of the identified tyrosine-containing peptides).
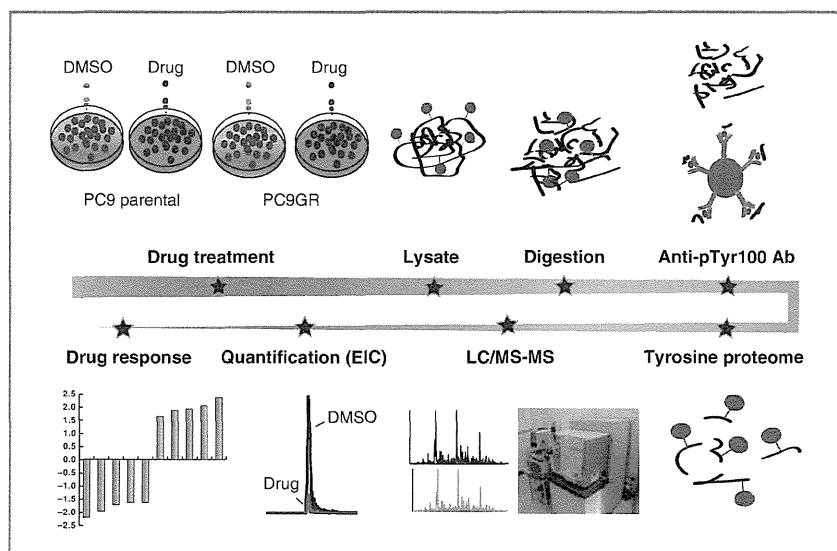
more abundant in the PC9GR cells, whereas 77 unique pTyr peptides (55 proteins) were less abundant in PC9GR cells than in PC9 cells. Compared with PC9 cells, PC9GR cells demonstrated increased amounts of pTyr peptides corresponding to numerous RTKs, some of which could be potential codrivers of resistance in PC9GR cells under the correct environmental circumstances. We observed a clear subnetwork characterized by hyperactive MET signaling (Fig. 2A, right) despite the lack of MET gene amplification. We observed nearly 11-fold more MET pTyr peptides in PC9GR than in PC9 cells. Similarly, we observed nearly >10-fold more pTyr peptides corresponding to ROR1 or neurotrophic tyrosine kinase receptor related-1 (pTyr-789, ~13-fold; pTyr-828, ~34-fold). ROR1 is a pseudokinase that cooperates with MET to promote tumorigenesis (35). Tyrosine phosphorylation of the MET adaptor proteins Gab1 and Gab2 were also more abundant in PC9GR cells.

In addition, pTyr peptides corresponding to the AXL RTK were increased approximately 8-fold in PC9GR cells. AXL upregulation has recently been shown to be a mechanism of acquired resistance of lung cancer cells to EGFR-TKI (36). Finally, increased abundance of multiple peptides corresponding to IRS2 (pTyr-675, 4.97-fold; pTyr-598, 5.47-fold; pTyr-823, 9.55-fold; pTyr-653, 19.93-fold; and pTyr-742, 21.29-fold), an adaptor protein linking insulin and insulin-like growth factor (IGF) signaling to PI3K signaling, was observed in PC9GR cells compared with parent PC9 cells. This suggested that either more insulin or IGF signaling exists in these cells or more IRS2 protein is expressed. We confirmed higher levels of tyrosine-phosphorylated MET and AXL in PC9GR than in PC9 cells and also found more total IRS2 protein in PC9GR than in PC9 cells (Fig. 2B). Despite the increased levels of MET signaling, we found minimal effects of combined MET-TKI (PHA665752) and EGFR-TKI (erlotinib or irreversible CL387,785) in PC9GR cells (Fig. 2C). While MET

signaling is hyperactivated, in this context, it is not responsible for affecting cell survival.

To examine whether changes of MET, IRS2, or AXL are driven specifically by T790M, we examined phosphorylation of these molecules in lung cancer cell lines (HCC4006 and HCC827) engineered to express an exon 19 E746-A750 + T790M allele. (Fig. 2B). We observed less pMET, less total MET, slightly more abundant pAXL, and similar total AXL in HCC4006-T790M cells compared with parent HCC4006 cells. We found equivalent pMET and total MET, less pAXL and equivalent total AXL in HCC827-T790M cells compared with parent HCC827 cells. The levels of IRS2 protein were unchanged across these HCC4006 and HCC827 cell lines unlike in PC9 and PC9GR cells. These results suggest that changes of MET, IRS2, or AXL are not dependent on EGFR-T790M but rather are likely to occur on a cell by cell basis.

Perturbations by EGFR-TKI identify downstream proteins and proteins involved in adaptive and microenvironment-derived responses

We next compared alterations in pTyr peptide abundance in both cell lines following erlotinib exposure (Supplementary Table S1). We identified pTyr peptides with >1.5-fold change differences from control (P < 0.05). In PC9 cells, we observed 31 less abundant and 45 more abundant unique pTyr peptides following 1 hour of erlotinib treatment (Fig. 3A). As expected, PC9GR cells displayed a more blunted response to erlotinib than PC9 cells; nonetheless, we did observe congruent changes in most pTyr peptides, thus increasing our confidence that these pTyr peptides and pathways are downstream of mutant EGFR given the expected biologic responses with cells harboring T790M mutations. Among the reduced pTyr peptides, we observed MK01, SHC1, GAB1, EGFR, and ERBB3 consistent with their known roles in ERBB signaling. Interestingly, we also observed reductions in peptides corresponding to Ras
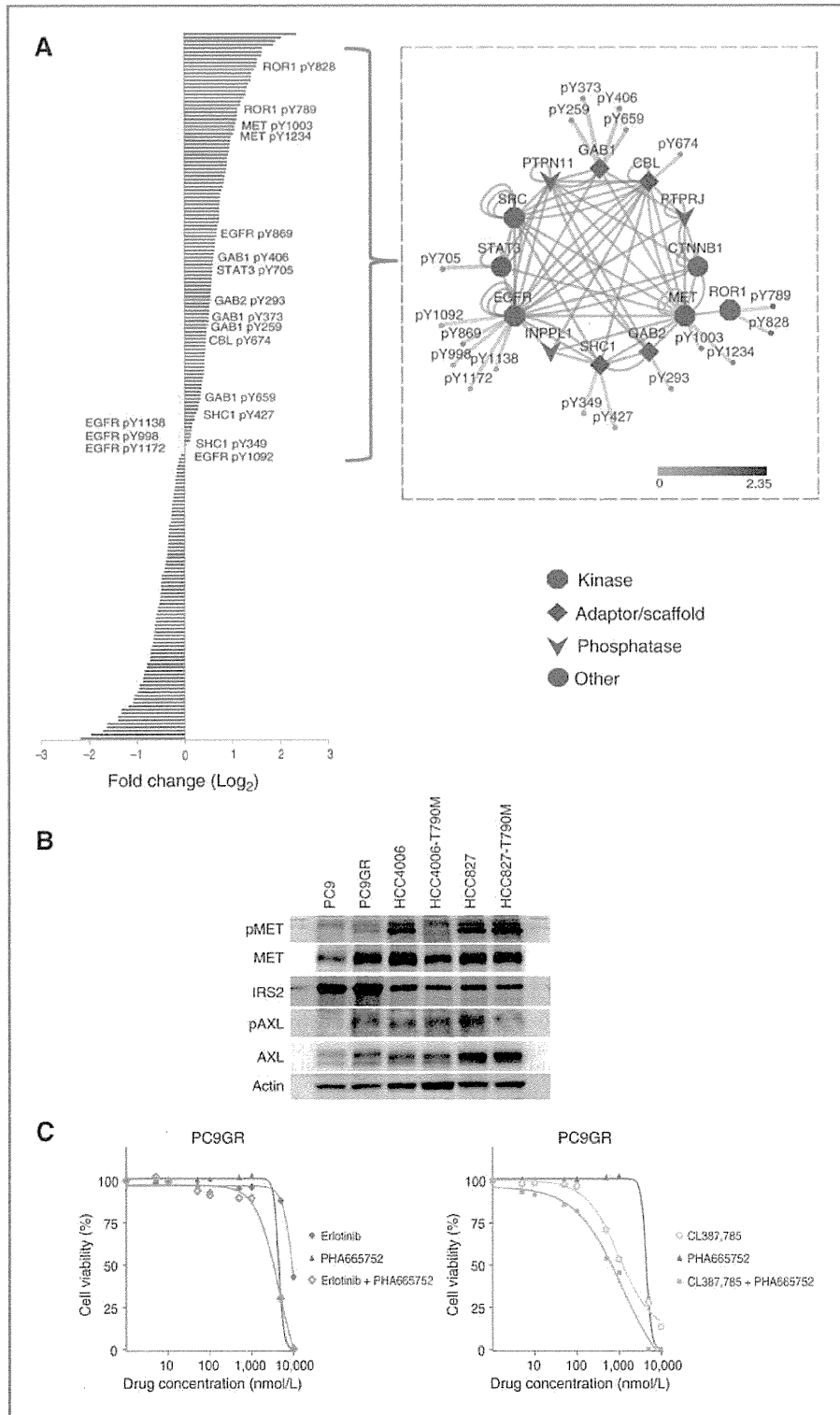
signaling, including SYGP1 or SynGAP, which can affect ERK and p38 MAPK functions in neurons (37, 38). Tyrosine-phosphorylated Rab7A (also known as Ras-related protein Rab-7a) was likewise reduced by erlotinib and has been linked to EGFR trafficking in endosomes (39).

Interestingly, we observed that nearly equal amounts of pTyr peptides were increased by erlotinib compared with peptides reduced by erlotinib (45 up and 31 down in PC9; 26 up and 30 down in PC9GR). We found more abundant pTyr peptides for IRS2, MET, YES, AXL, FAK, ERBB2, and BRK (PTK6) following erlotinib treatment, and this pattern was consistent across both PC9 and PC9GR cells (Fig. 3B). We hypothesized that the increased levels of RTK identified through our approach could cooperate with exogenous ligands and promote EGFR-TKI resistance. Recent studies have highlighted the ability of growth factor ligands to promote resistance to targeted agents (23–25). We therefore tested if the increased pTyr in key RTK could cooperate with growth factor ligands to drive resistance to EGFR-TKI. We incubated PC9 and PC9GR cells with cognate ligands corresponding to the upregulated RTK in PC9GR, including IGF1, hepatocyte growth factor (HGF), and GAS6 (the ligand for AXL RTK), and determined the effects on erlotinib sensitivity in PC9 cells and afatinib sensitivity in PC9GR cells (Fig. 3C). Interestingly, HGF and IGF but not GAS6 had protective effects on both PC9 cells exposed to erlotinib and PC9GR cells exposed to afatinib. In PC9 cells, the shift in IC_{50} was rather modest; however, in PC9GR cells, the effect was more dramatic. This shift pattern was consistent between both cell lines, with HGF having more of an effect than IGF1, whereas no effect was seen with activation of AXL by GAS6 in these cells. Using Western blotting, we examined the effects of these ligands on EGFR signaling with or without EGFR-TKI in both PC9 and PC9GR cells. HGF activated pMET in both PC9 and PC9GR cells (Supplementary Fig. S5A and S5B). This HGF-induced activation of pMET and downstream pAkt and pErk were not inhibited by erlotinib in PC9 or by afatinib in PC9GR cells (Supplementary Fig. S5A and S5B). These results also suggest that MET activation in PC9 and PC9GR cells is not dependent on EGFR signaling. On the other hand, we did not observe clear ligand-dependent activation of corresponding RTKs or sustained activation of pAkt and pErk in the presence of EGFR-TKIs in IGF1-induced or Gas6-induced PC9 and PC9GR cells (Supplementary Fig. S5C–S5F). These results are consistent with our data showing that IGF1 and Gas6 had less

rescue effects compared with HGF in these cells (see Fig. 3C). These results suggest that altered RTK identified by phosphoproteomics can be codrivers of resistance under specific environmental circumstances. Furthermore, the increased levels of multiple RTKs in response to erlotinib suggest innate priming of RTK, where RTKs are primed to cooperate with growth factor ligands through intracellular mechanisms.

Afatinib combined with dasatinib inhibits EGFR signaling more efficiently than either agent alone in TKI-resistant NSCLC cells with T790M

We reexamined our data for pTyr peptides that were not perturbed by EGFR-TKI and were not different between the PC9 and PC9GR cell lines. We hypothesized that this analysis may uncover parallel signaling pathways that cooperate with EGFR to maintain cellular growth and/or survival. We identified 31 proteins that fulfilled this criterion, including multiple SFKs as well as CSK, PKCD, MAPK3, PIK3R2, SYK, TNK2, EPHB2, EPHA4, FAK, and PTK2B. We observed no changes in pTyr peptides corresponding to SFKs, including the pTyr peptide LIEDNEy-TAR corresponding to the common autocatalytic site in c-SRC, YES, and FYN, following EGFR-TKI, suggesting this as an EGFR-independent pathway. We linked SFK proteins to other proteins found in our entire dataset through interaction databases (Fig. 4A), identifying a large group of proteins ($N = 28$) with reported interactions with SFK proteins (gray circles) that were also unchanged by erlotinib. In addition, we identified potential interactions between SFK and proteins either altered by erlotinib (gray parallelogram and diamond) or altered in PC9GR compared with PC9 cells (gray V and diamond). For example, SRC can cooperate with EGFR, MET, ERBB3, SHC1, CBL, and STAT3 signaling nodes (gray parallelogram) that we previously identified as being altered by erlotinib and different between PC9 and PC9GR cells.

On the basis of this observation, we hypothesized that cotargeting SFKs and EGFR T790M with dasatinib and afatinib, respectively, may produce additive or synergistic anti-tumor effects. Furthermore, our previous studies suggested that the antitumor effects of dasatinib are mediated in part by direct EGFR inhibition that is mitigated by gain of T790M in EGFR (32). However, these studies also suggested that irreversible EGFR-TKIs combined with dasatinib could

---

Figure 2. Phosphoproteins associated with T790M-mediated resistance. A, connectivity of MET protein was determined using protein–protein interaction databases to better aid in visualizing differentially expressed proteins that may be associated with PC9GR cells. The left histograph shows change of pTyr sites in PC9GR cells compared with in PC9 cells. The fold change ($P < 0.05$, fold change > 1.5) of all tyrosine peptides were presented in log_2 scale. Red bar shows the tyrosine phosphosites of MET network proteins in PC9GR cells. Right, the MET network. Statistically decreased or increased pTyr peptides were input into Cytoscape 2.8.3, and protein–protein interactions were identified using InnateDB based on molecular interactions and functional relations from public sources. Shapes reflect types of proteins shown in figure. Pink circle represents the pTyr peptides significantly different between PC9 and PC9GR cells and different between erlotinib-treated and control cells ($P < 0.05$; fold change >1.5). Color scale corresponds to fold change in Log2 scale. The yellow lines represent the direct interaction with MET. B, Western blotting of selected proteins in PC9, PC9GR, HCC4006, HCC4006-T790M, HCC827, HCC827-T790M cells. Membranes were blotted with pTyr 1234/1235 MET, total MET, pTyr 702 AXL, total AXL, and total IRS2 antibodies in PC9, PC9GR, HCC4006, HCC4006-T790M, HCC827, HCC827-T790M cells with actin confirming equal protein loading. C, PC9GR cells were treated for 72 hours with increasing concentrations of erlotinib alone, CL387,785 alone, PHA665752 alone, erlotinib + PHA665752, or CL387,785 + PHA665752. Data generated by cell viability assay (CellTiter-Glo) are expressed as a percentage of the value for untreated cells. Determinations were done in triplicate. Please view online version for full details.
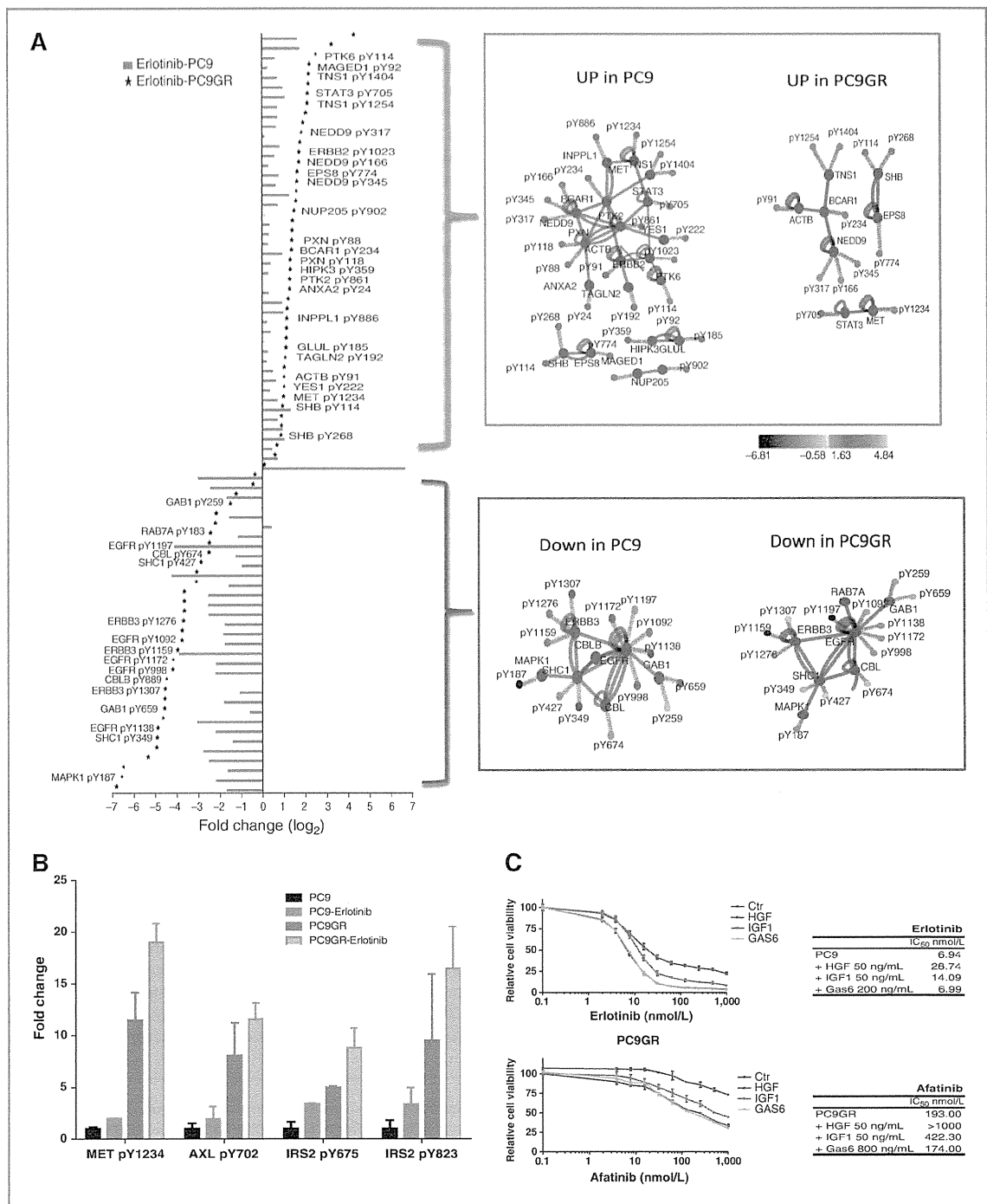

Figure 3. Erlotinib perturbations in PC9 and PCGR cell lines. A, effects of erlotinib on tyrosine containing phosphoproteomes in PC9 and PC9GR cell lines. Left, erlotinib-induced changes (*P* < 0.05; fold change >1.5) of pTyr sites in PC9 (bars) and PC9GR (*) cells. Four subnetworks were created within different catalog proteins (blue circle) based on increased or decreased pTyr sites in PC9 and PC9GR cells. Color scale represents the fold change of each pTyr site. B, pTyr peptide abundance measured by EIC across erlotinib-treated PC9 and PC9GR cells for MET, AXL, and IRS2 pTyr peptides. Y-axis indicates fold change above PC9 untreated pTyr abundance. C, PC9 or PC9GR cells were seeded in 96-well plates for 24 hours and then exposed to HGF or IGF1 (50 ng/mL) or GAS6 (200 ng/mL) and concomitantly exposed to increasing concentrations of relevant kinase inhibitor. After 72 hours, cell viability was assessed. IC$_{50}$ was calculated for each condition. Please view online version for full details.

inhibit EGFR T790M. Thus, we examined the effects of erlotinib, afatinib, dasatinib, or combined afatinib and dasatinib on EGFR signaling in PC9GR and H1975 cells, both resistant cell lines against EGFR-TKI because of T790M (Fig. 4B). In both cell lines, erlotinib inhibited neither EGFR nor SFKs, and no complete suppression of pAkt and pErk (both essential downstream molecules of EGFR) was observed. We found that afatinib could inhibit pEGFR; however, SFKs were again unaltered. These results with erlotinib and afatinib are consistent with our pTyr mass spectrometry results that detected no changes in pTyr SFKs following erlotinib exposure. We also found that combining afatinib and dasatinib resulted in more efficient inhibition of pAkt and pErk in PC9GR and H1975 cells than each agent alone, suggesting that SFKs are cosignals related to EGFR T790M and that irreversible EGFR-TKIs combined with SFKs more efficiently block EGFR signaling in NSCLC cells harboring T790M.

Afatinib combined with dasatinib effectively inhibits cell growth and significantly increases apoptotic cells in TKI-resistant NSCLC cells with T790M

Given that the combination of afatinib and dasatinib efficiently inhibited EGFR signaling in NSCLC cells harboring T790M, we examined the effects of this combination on cell proliferation and apoptosis in PC9GR and H1975 cells. We found reduced IC_{50} levels in PC9GR and H1975 cells versus either agent alone (Fig. 4C; Supplementary Tables S2 and S3). We examined the effects of combining afatinib plus dasatinib in other NSCLC cells with T790M (HCC4006-T790M and HCC827-T790M cells), cells with TKI-sensitive EGFR mutation only (PC9, HCC4006, and HCC827 cells), and cells with wild-type EGFR (H460, A549, and H1299 cells). We observed reduced IC_{50} for afatinib plus dasatinib versus either agent alone in HCC4006-T790M and HCC827-T790M cells (Supplementary Fig. S6), whereas curves for this combination were mostly overlapped with those for afatinib or dasatinib alone in PC9, HCC4006, and HCC827 cells with TKI-sensitive EGFR mutation only (Supplementary Fig. S7) or H460, A549, and H1299 cells with wild-type EGFR (Supplementary Fig. S8). We also found that dasatinib combined with CL387,785, another irreversible EGFR-TKI, reduced IC_{50} versus either agent alone in PC9GR cells (Supplementary Fig. S9). Furthermore, we also detected more apparent PARP cleavage when agents were combined than when used alone or when cells were erlotinib treated (see Fig. 4B). Similar to results with afatinib, when we examined the effects of combined dasatinib with WZ4002, another T790M-specific EGFR-TKI (40), IC_{50} was reduced versus when agents were used alone (Fig. 4D; Supplementary Tables S2 and S3).

Rescue experiments revealed that dasatinib enhanced antitumor effects of afatinib by inhibition of SRC and FYN

Although our clustering approach and dasatinib results strongly implicated SFKs as the key target, we examined this in more detail given the extensive promiscuousness of dasatinib. Using dasatinib-insensitive alleles expressed in lentiviral vectors, we investigated whether dasatinib-resistant forms of key SFKs could rescue effects of dasatinib (32). To test which SFK is critical as a dasatinib target in NSCLC cells harboring T790M when combined with afatinib, we infected cells with lentivirus expressing either wild-type kinases or kinase alleles with drug-resistant gatekeeper mutations of SFKs (SRC, LYN, FYN, and FRK) and examined cell viability in response to increasing concentrations of dasatinib plus afatinib (Fig. 4E). Our results show that SRC and FYN were able to rescue PC9GR cells from dasatinib plus afatinib. However, no effects were observed with LYN and FRK, suggesting that SRC and FYN are essential SFKs as dasatinib targets in NSCLC cells with T790M.

Dasatinib enhances the antitumor activity of afatinib in vitro and in vivo

To evaluate more formally whether our combination effects were because of additional cell death, we measured caspase-3–positive cells following TKI treatment (Fig. 5A). In PC9GR cells, both erlotinib and dasatinib had no effects on apoptosis, but the combination had modest effects. Afatinib led to more apoptosis, which was further increased when combined with dasatinib. Similar effects of afatinib plus dasatinib on apoptosis were observed in HCC4006-T790M and HCC827-T790M cells (Supplementary Fig. S10). WZ4002 also induced apoptosis as a single agent, which was potentiated when combined with dasatinib. In H1975 cells, similar effects were observed, with dasatinib increasing apoptosis when added to afatinib and WZ4002. These results indicate that Src inhibitors enhance antiproliferative and proapoptotic effects of irreversible or T790M-selective EGFR-TKIs in NSCLC cells with T790M.

We hypothesized that the enhanced apoptosis with combined afatinib and dasatinib would translate into improved in vivo effects on tumor growth. We examined the antitumor effects of this combination in mouse xenograft models with PC9GR cells. As single agents, afatinib (10 mg/kg) or dasatinib (15 mg/kg) had modest effects on inhibiting tumor growth in PC9GR xenografts; however, when combined, we observed significantly greater inhibition of growth, including tumor regression consistent with our apoptosis results (Fig. 5B). These results demonstrate that Src inhibitors effectively enhance antitumor effects of irreversible EGFR-TKI in gefitinib-resistant NSCLC xenografts with T790M, providing a rationale to evaluate this strategy in patients with NSCLC who have acquired EGFR-TKI resistance related to T790M.

Tyrosine phosphoproteomes in lung adenocarcinoma samples with TKI-sensitive EGFR mutations

To validate that our cell line models and data are applicable to human lung cancer tissues, we conducted a mass spectrometry tyrosine phosphoproteomics analysis on four NSCLC tumor samples with TKI-sensitive EGFR mutations. In total, we identified 279 unique pTyr sites corresponding to 189 unique proteins across all four tumor samples. For each tumor, we identified 158, 153, 157, and 109 unique